energies

MDPI

Article

Bilevel Stochastic Low-Carbon Operation Optimization of Integrated Energy Systems Based on Dynamic Mean–Conditional Value at Risk (CVaR) and Stepwise Carbon Trading Mechanism

Jing Zhang [1], Xinyi He [1], Jianfei Li [1], Diyu Chen [1], Yingang Ye [1], Shumei Chu [2,*], Xinhong Cheng [2] and Fei Zhao [2]

[1] Taizhou Hongyuan Electric Power Design Institute Co., Ltd., Taizhou 318000, China
[2] Department of Electric Power Engineering, North China Electric Power University, Baoding 071003, China; 220242213242@ncepu.edu.cn (X.C.); zhaofei@ncepu.edu.cn (F.Z.)
* Correspondence: chushumei@ncepu.edu.cn

Abstract

To enhance the low-carbon operational performance of integrated energy systems (IESs) under multi-source uncertainties, this study proposes a bilevel stochastic optimization framework incorporating a dynamic mean–CVaR risk model and a tiered carbon pricing mechanism. The upper level adopts an improved NSGA-II to jointly optimize economic cost, carbon emissions, and system flexibility through capacity planning decisions. The lower level performs scenario-based operation evaluation with a time-varying risk aversion coefficient, enabling differentiated risk responses across operating periods. A stepwise carbon price function and a capped carbon revenue mechanism are introduced to represent real carbon market regulations and avoid excessive emission reduction benefits. Multidimensional uncertainty scenarios—covering renewable variability, load fluctuations, and market price disturbances—are generated for risk-aware evaluation. Simulation results show that the proposed approach effectively reduces cost and emission volatility and achieves a more balanced trade-off between economy and low-carbon performance compared with conventional static-risk models. Sensitivity analyses further reveal that increased risk aversion shifts system operation strategies from economy-oriented to robustness-oriented modes, highlighting the importance of dynamic risk modeling and carbon policy design for future low-carbon multi-energy systems.

Keywords: integrated energy system; dynamic risk modeling; mean–CVaR; tiered carbon-pricing mechanism; bilevel stochastic optimization

Check for updates

Academic Editor: Seung-Hoon Yoo

Received: 6 February 2026
Revised: 4 March 2026
Accepted: 9 March 2026
Published: 12 March 2026

Copyright: © 2026 by the authors. Licensee MDPI, Basel, Switzerland. This article is an open access article distributed under the terms and conditions of the Creative Commons Attribution (CC BY) license.

1. Introduction

With the acceleration of global decarbonization and the advancement of energy digitalization, integrated energy systems (IESs) has emerged as a promising paradigm for enhancing energy efficiency and facilitating multi-energy coupling among electricity, natural gas, hydrogen, and heat networks [1]. The integration of power-to-gas (P2G), carbon capture and storage (CCS), and hydrogen technologies enables flexible energy conversion and long-term storage, providing critical support for renewable-energy accommodation and carbon neutrality targets [2–5]. In particular, policy-driven multi-energy coordination mechanisms have demonstrated significant impacts on system-level economic and environmental performance [6].

However, the increasing penetration of renewable generation introduces substantial uncertainties in energy production, load demand, and market prices. These uncertainties

significantly affect operational reliability and economic returns, making risk-aware optimization an essential requirement in modern IES planning and dispatch [7,8]. Conditional Value at Risk (CVaR), as a coherent risk measure proposed by Rockafellar and Uryasev [9], has been widely applied in power system risk management due to its ability to capture tail loss behavior under extreme scenarios. Morales et al. [10] demonstrated the effectiveness of risk-based valuation in wind-integrated power systems, highlighting the necessity of considering extreme events in dispatch decisions.

Recent studies have incorporated CVaR into virtual power plant bidding [8], energy storage operation [11], integrated energy scheduling [12,13], and multi-level distributed energy management [14]. Dynamic risk-adjustable formulations have also been explored to address time-varying risk preferences [15–17], while chance-constrained and risk-adjustable goal programming models have further extended stochastic energy optimization frameworks [18]. These works confirm that risk-averse modeling significantly enhances system robustness under multi-scenario uncertainties.

In parallel, bilevel optimization has been extensively adopted to represent hierarchical decision structures in energy systems. Ran et al. [19] developed a bilevel regional IES model under climate change uncertainty. Aljohani et al. [20] proposed a trilevel coordinated framework for large-scale EV charging. Zhao et al. [21] and Li et al. [22] investigated carbon-aware bilevel dispatch in electricity–gas systems. More recently, Lu et al. [23] and Zhou et al. [24] extended bilevel planning to electricity–hydrogen systems with renewable uncertainty and seasonal hydrogen storage. These studies demonstrate that bilevel models effectively capture the interaction between upper-level planning and lower-level operational responses.

Nevertheless, most existing bilevel models adopt either deterministic or static risk parameters, which may fail to reflect temporal variation in risk attitudes. Moreover, although carbon trading has been integrated into IES optimization, its treatment often assumes linear pricing or simplified mechanisms.

Carbon trading and stepped carbon pricing mechanisms have become critical policy tools for low-carbon transformation. Rehman et al. [25] and Tao et al. [26] investigated stepped carbon trading in integrated energy scheduling. Tanveer et al. [27] analyzed innovative carbon pricing and market coupling practices. Kong et al. [28] and Jiang et al. [29] explored step-based pricing in CCUS and park-level IES planning. In addition, recent works have incorporated carbon trading into electricity–gas virtual power plants [30], electricity–hydrogen dispatch models [31,32], and demand-response-coupled systems [33]. These studies reveal that progressive carbon pricing significantly influences technology configuration and dispatch strategies.

Despite these advances, three major gaps remain in the current literature:

1. Most CVaR-based IES models adopt static risk coefficients, lacking dynamic risk adjustment mechanisms to reflect temporal uncertainty characteristics.
2. Existing carbon trading models rarely incorporate revenue cap mechanisms under stepped pricing schemes, which may distort carbon market incentives.
3. Comprehensive stochastic bilevel optimization frameworks that jointly integrate dynamic risk modeling, stepped carbon trading, and multi-energy coupling remain limited.

To address these gaps, this paper proposes a bilevel multi-objective optimization framework for IESs that integrates dynamic mean–CVaR risk modeling with a refined stepwise carbon pricing mechanism. The upper level optimizes key planning parameters—such as photovoltaic capacity, electrolyzer ratings, hydrogen storage scale, P2G capacity, and CCS efficiency—under the objectives of minimizing net cost, carbon emissions, and maximizing operational flexibility. The lower level evaluates risk-adjusted operational

performance through scenario simulations with time-varying risk weights derived from load peak–valley characteristics. A stepwise carbon pricing model with revenue capping is incorporated to reflect realistic carbon market regulations. Furthermore, 300 Monte Carlo robustness scenarios are used for abnormal-scheme elimination via Z-score and IQR detection, and a TOPSIS-based decision method is applied to select robust and well-balanced solutions.

2. Model Framework and Mathematical Description

2.1. Bilevel Stochastic Formulation

The IES consists of photovoltaic/wind generation, electrolyzers, hydrogen storage, P2G methanation, CCS units, and conventional gas supply equipment. Through electricity–gas–hydrogen coupling, the system forms a coordinated multi-energy conversion pathway that supports low-carbon operation.

As shown in Figure 1, renewable energy first supplies electrical demand; surplus electricity is converted into hydrogen and stored. Hydrogen can be discharged for power generation or converted into methane via P2G during peak-load periods to enhance flexibility. CCS captures CO_2 from gas-fired units and electrolysis. Captured CO_2 is partly reused in methanation ($CO_2 + 4H_2 \rightarrow CH_4 + 2H_2O$) and partly sequestered, forming a closed-loop electricity–gas–carbon pathway and reducing net emissions.

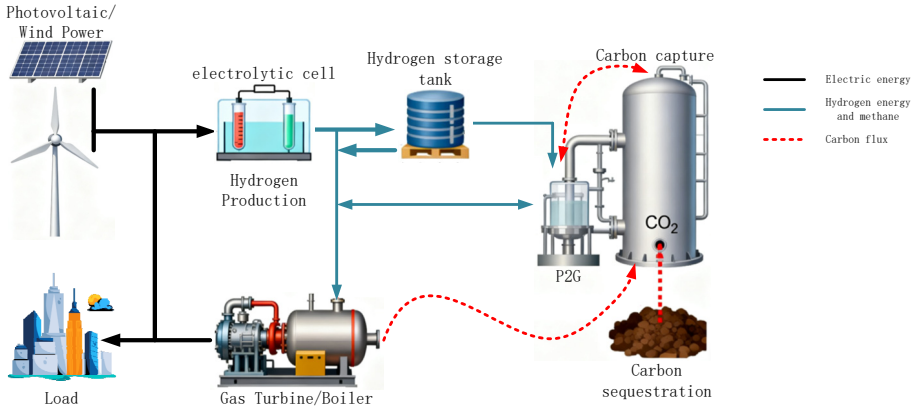


Figure 1. Physical energy and carbon flow structure of the integrated energy system.

This study adopts a closed-loop bilevel structure combining upper-level planning and lower-level operational evaluation under multi-source uncertainties (renewable fluctuations, energy market disturbances, carbon price volatility). A stepwise carbon pricing mechanism is embedded to incorporate carbon market feedback into the optimization process.

For each upper-level candidate solution x, uncertainty scenarios $\{\xi_S\}_{S=1}^{S}$ are generated via Monte Carlo/LHS sampling. Under each scenario, the lower-level operational optimization problem is solved to obtain the optimal response $y_S^*(x)$. The scenario-wise optimal outcomes $Cs(x)$,$Es(x)$ are aggregated via mean–CVaR to construct the upper-level objective vector $F(x)$, which guides the evolutionary search.

Lower-layer model (operation layer): Based on upper-level decisions, multi-scenario simulations are generated using Monte Carlo sampling considering electricity, gas, and carbon price fluctuations as well as renewable variability. A dynamic mean–CVaR model evaluates cost and emissions under uncertainty.

In addition, a stepwise carbon pricing mechanism is introduced to capture the dynamic incentive effects of real carbon trading policies. When annual net emissions exceed a preset threshold, carbon prices increase according to segmented increments; when negative

emissions occur, carbon revenues decrease following the same principle. To prevent unrealistic profits, a carbon revenue upper bound ($\leq$0.8 $\times$ total cost) is imposed.

The overall model logic consists of the following:

(1) Upper-layer optimization $\rightarrow$ generate planning solutions;
(2) Lower-layer simulation $\rightarrow$ evaluate risk under multi-scenario disturbances;
(3) Risk feedback $\rightarrow$ compute dynamic mean–CVaR indicators;
(4) Multi-criteria decision-making $\rightarrow$ eliminate abnormal solutions and rank valid schemes using TOPSIS.

This architecture implements a closed-loop synergy of "capacity planning–operational scheduling–carbon market feedback," enabling quantitative evaluation of carbon trading impacts and the dynamic balance among risk preference, emission limits, and system flexibility. Compared with traditional single-layer CVaR models, the proposed approach offers notable advantages in time-varying risk modeling, nonlinear carbon price responses, and multi-energy collaborative optimization. The overall structure of the proposed bilevel stochastic optimization framework and the interaction between the planning layer and the operational layer are illustrated in Figure 2.

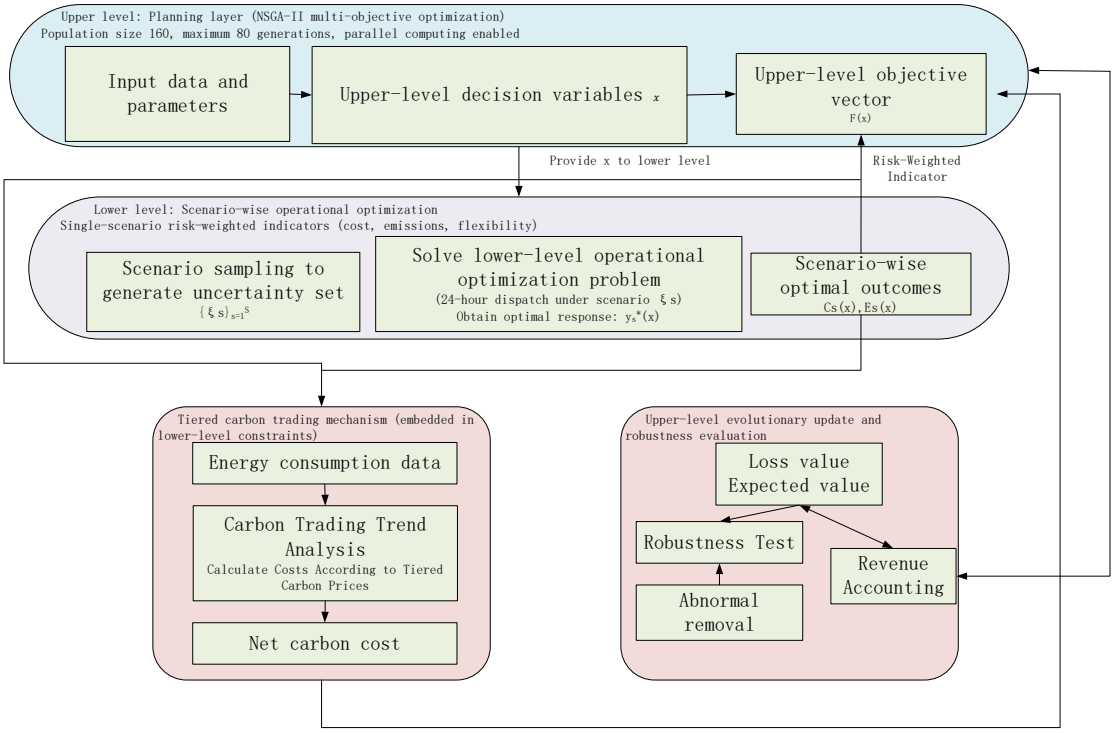


Figure 2. Bilevel stochastic optimization framework with scenario-wise lower-level optimal response.

2.2. Upper-Layer Optimization Objectives

The upper-level planning decision vector is

$$x = \left[P_{\text{renew}}, \overline{P}_{\text{ely}}, \overline{H}_2, r_{\text{ccs}}, \overline{P}_{\text{p2g}}, \theta_{\text{NG}}, \eta_{\text{NH3}}, \phi_{O_2}\right], \quad (1)$$

where P_{renew}(kW): installed renewable capacity; $\overline{P}_{\text{ely}}$(kW): electrolyzer capacity; $\overline{H}_2$(kg): hydrogen storage size; $r_{\text{ccs}} \in [0, \gamma_{\max}]$: CCS capture rate decision; $\overline{P}_{\text{p2g}}$(kW): P2G capacity; $\theta_{\text{NG}} \in [0,1]$: natural-gas blending ratio parameter; $\eta_{\text{NH3}} \in [0,1]$: ammonia synthesis efficiency; $\phi_{O_2} \in [0, 0.25]$: oxygen fraction affecting CCS efficiency.

These planning variables enter the lower-level feasible region through capacity bounds and physical coupling constraints, thus forming a genuine bilevel coupling.

For each scenario ξs, the lower-level operational optimization yields the optimal response $y_s^*(x, \xi_s)$. The corresponding scenario-wise outcomes are defined as

$$C_s(x) = C(x, y_s^*(x, \xi_s); \xi_s), \quad E_s(x) = E(x, y_s^*(x, \xi_s); \xi_s). \tag{2}$$

The expectations are

$$\mathbb{E}[C(x)] = \frac{1}{S}\sum_{s=1}^{S} C_s(x), \quad \mathbb{E}[E(x)] = \frac{1}{S}\sum_{s=1}^{S} E_s(x). \tag{3}$$

Let $\alpha \in (0,1)$ be the confidence level. The Conditional Value at Risk (CVaR) of cost is defined as

$$\mathrm{CVaR}_\alpha(C(x)) = \min_{z\in\mathbb{R}} \left[z + \frac{1}{(1-\alpha)S}\sum_{s=1}^{S} \max(0,\ C_s(x) - z) \right] \tag{4}$$

and similarly $\mathrm{CVaR}_\alpha(E(x))$. The upper-level risk-adjusted objectives use the mean–CVaR formulation

$$\begin{aligned} J_C(x) &= (1-\omega)\mathbb{E}[C(x)] + \omega\ \mathrm{CVaR}_\alpha(C(x)), \\ J_E(x) &= (1-\omega)\mathbb{E}[E(x)] + \omega\ \mathrm{CVaR}_\alpha(E(x)), \end{aligned} \tag{5}$$

where $\omega \in [0, 1]$ is the mean–CVaR trade-off coefficient (global planning risk preference).

Finally, together with the flexibility objective (Section 2.6), the upper-level multi-objective vector is

$$F(x) = [J_C(x),\ J_E(x),\ -\mathbb{E}[\mathrm{Flex}(x, \xi_s)]]. \tag{6}$$

2.3. Uncertainty Modeling and Scenario Generation

A scenario ξs collects the uncertain factors

$$\xi_s = \left(\pi_s^e,\ \pi_s^g,\ \pi_s^{CO2},\ \gamma_s^{\mathrm{grid}},\ \rho_{t,s} \right) \tag{7}$$

where π_s^e is electricity price, π_s^g is gas price, π_s^{CO2} is carbon price level (used in stepwise pricing), γ_s^{grid} is grid emission factor, and $\rho_{t,s}$ is the renewable profile multiplier (dimensionless, hourly profile scaling factor).

To ensure physical consistency and reproducibility, uncertainties are modeled as multiplicative disturbances around baseline values:

$$\begin{aligned} &\pi_s^e = \pi^e(1+\varepsilon_s^e), \quad \pi_s^g = \pi^g(1+\varepsilon_s^g), \\ &\pi_s^{CO2} = \pi^{CO2}(1+\varepsilon_s^c), \\ &\gamma_s^{\mathrm{grid}} = \gamma^{\mathrm{grid}}(1+\varepsilon_s^\gamma), \\ &\rho_{t,s} = \mathrm{clip}\left(\rho_t(1+\varepsilon_s^\rho), 0, 2\right) \end{aligned} \tag{8}$$

where $\varepsilon_s = \left[\varepsilon_s^e, \varepsilon_s^g, \varepsilon_s^c, \varepsilon_s^\gamma, \varepsilon_s^\rho\right]^T$ is the standardized disturbance vector.

Each disturbance component is assumed dimensionless and characterized by the following standard deviations:

$$\sigma = [\sigma^e, \sigma^g, \sigma^c, \sigma^\gamma, \sigma^\rho] = [0.20,\ 0.20,\ 0.25,\ 0.25,\ 0.25] \tag{9}$$

These values represent coefficients of variation and are consistent with commonly reported uncertainty ranges in integrated energy system studies:

Electricity and gas price volatility in energy markets frequently exhibits fluctuations exceeding ±15–20%. Carbon price volatility under emissions trading systems is often higher and can exceed ±20%. Renewable-output forecast errors and system-level renewable-penetration variability commonly range between 15 and 25%. Grid emission factor variation due to fuel mix changes can exceed 10–20% depending on seasonal and system conditions.

Therefore, the adopted uncertainty levels represent a moderate-to-conservative stress test suitable for planning-level stochastic optimization.

Historical observations of these variables are collected over a representative time window. Let $u_t \in \mathbb{R}^5$ denote the standardized perturbation vector at sample n, obtained from relative deviations or log-returns after de-trending and normalization. The correlation matrix is estimated as

$$R_{ij} = \mathrm{corr}(u_i, u_j), \tag{10}$$

To incorporate both correlation and marginal dispersion, the covariance matrix is constructed as

$$\Sigma = DRD \tag{11}$$

where $D = diag(\sigma)$.

Thus

$$\varepsilon_s \sim \mathcal{N}(0, \Sigma) \tag{12}$$

This formulation ensures correct marginal standard deviations and preserved cross-variable dependence.

In this study, π_s^e, π_s^g, π_s^{CO2}, γ_s^{grid} are regarded as daily scalars categorized by scenario, remaining unchanged over the 24 h scheduling horizon. Renewable-energy uncertainty is implemented as a daily multiplicative scaling factor applied to the deterministic hourly renewable-energy profile ρt. The design maintains the intraday deterministic shape of renewable energy while introducing stochastic variation in overall renewable-energy availability, which is suitable for planning-level stochastic analysis.

Scenario generation follows two steps:

Step 1: Draw correlated disturbance samples $\varepsilon_s \sim \mathcal{N}(0, \Sigma)$.

Step 2: Map disturbances to scenario parameters.

The multiplicative mapping equations defined above generate the scenario parameters ξ_s. The same correlated scenario set is used consistently when comparing dynamic β_t vs. static β and different global risk weight settings, to ensure fairness in risk comparison.

For reproducibility, a fixed random seed is used during scenario generation.

The lower level optimizes a 24 h dispatch with decision variables:

$$R = \begin{bmatrix} 1 & 0.40 & 0.55 & 0.60 & -0.50 \\ 0.40 & 1 & 0.35 & 0.30 & -0.30 \\ 0.55 & 0.35 & 1 & 0.65 & -0.45 \\ 0.60 & 0.30 & 0.65 & 1 & -0.50 \\ -0.50 & -0.30 & -0.45 & -0.50 & 1 \end{bmatrix} \tag{13}$$

For a fixed x and scenario ξs, the lower level optimizes a 24 h dispatch with decision variables:

$$y_s = \left\{ p_{t,s}^{\mathrm{ely}},\ p_{t,s}^{\mathrm{ng}},\ p_{t,s}^{\mathrm{p2g}},\ h_{t,s}^{\mathrm{dis}},\ soc_{t,s} \right\}_{t=1}^{T} \cup \left\{ R_s^{\mathrm{prod}},\ R_s^{\mathrm{CO2}},\ F_s^{\mathrm{buy}},\ F_s^{\mathrm{sell}},\ \left\{ \delta_{k,s}^{\mathrm{buy}} \right\}_{k=1}^{K},\ \left\{ \delta_{k,s}^{\mathrm{sell}} \right\}_{k=1}^{K} \right\} \tag{14}$$

where $p_{t,s}^{\mathrm{ely}}$ (kW): electrolyzer power; $p_{t,s}^{\mathrm{ng}}$ (kW): natural-gas dispatch; $p_{t,s}^{\mathrm{p2g}}$ (kW): P2G power; $h_{t,s}^{\mathrm{dis}}$ ($\mathrm{kWhH_2/h}$): hydrogen discharge (energy-equivalent); $soc_{t,s}$ ($\mathrm{kWhH_2}$): hydrogen state of charge; R_s^{prod} (CNY/yr): product revenue (NH_3 + CH_4); R_s^{CO2} (CNY/yr): carbon trading

revenue; F_s^{buy}, F_s^{sell} (tCO_2/yr): allowance purchase/sale; $\delta_{k,s}^{\text{buy}}$, $\delta_{k,s}^{\text{sell}}$ (tCO_2/yr): piecewise variables for carbon trading segments.

The lower-level scenario-wise operational objective is

$$\min_{y_s} C_s(x, y_s; \xi_s) \tag{15}$$

with the following linear form consistent with the implemented LP:

$$C_s(x, y_s; \xi_s) = \sum_{t=1}^{T} \left(c_{t,s}^{\text{ely}} p_{t,s}^{\text{ely}} + c_{t,s}^{\text{p2g}} p_{t,s}^{\text{p2g}} + c_{t,s}^{\text{ng}} p_{t,s}^{\text{ng}} \right) + \sum_{k=1}^{K} \pi_k^{CO2} \delta_{k,s}^{\text{buy}} - R_s^{\text{prod}} - R_s^{\text{CO2}} \text{ (Cost)} \tag{16}$$

Electricity-related coefficients are risk-weighted by the operational-layer time-varying factor $1 + \beta_t$ (Section 2.4) and annualized by $N_d = 365$:

$$c_{t,s}^{\text{ely}} = c_{t,s}^{\text{p2g}} = \pi_s^e (1 + \beta_t) N_d, \quad c_{t,s}^{\text{ng}} = \pi_s^g N_d \tag{17}$$

(1) Capacity coupling and bounds (bilevel coupling)

Upper-level capacities impose bounds

$$0 \le p_{t,s}^{\text{ely}} \le \overline{P}_{\text{ely}}, \quad 0 \le p_{t,s}^{\text{p2g}} \le \overline{P}_{\text{p2g}}, \quad 0 \le soc_{t,s} \le \overline{H}_2 \cdot LHV_{H_2}, \quad \forall t \tag{18}$$

(2) Hourly supply–demand balance (equality)

Let L_t be the load at hour t. Renewable available power equals $P_{\text{renew}} \rho_{t,s}$. The balance is

$$p_{t,s}^{\text{ely}} + p_{t,s}^{\text{p2g}} - p_{t,s}^{\text{ng}} - \eta^{H2 \to P} h_{t,s}^{\text{dis}} = P_{\text{renew}} \rho_{t,s} - L_t, \quad \forall t \tag{19}$$

(3) Hydrogen storage dynamics and discharge feasibility

$$\begin{aligned} &soc_{t,s} - soc_{t-1,s} - \eta^{\text{ely}} p_{t,s}^{\text{ely}} + h_{t,s}^{\text{dis}} = 0, \quad \forall t \\ &0 \le h_{t,s}^{\text{dis}} \le soc_{t,s}, \quad \forall t \end{aligned} \tag{20}$$

(4) Product revenue constraint and revenue cap

The annual product revenue is bounded by a linear production proxy and by a fraction of total cost:

$$\begin{aligned} R_s^{\text{prod}} &\le \kappa_{\text{prod}}(x) \sum_{t=1}^{T} \left(p_{t,s}^{\text{ely}} + p_{t,s}^{\text{p2g}} \right) \\ R_s^{\text{prod}} &\le \gamma_{\text{prod}} \left(\sum_{t=1}^{T} c_{t,s}^{\text{ely}} p_{t,s}^{\text{ely}} + \sum_{t=1}^{T} c_{t,s}^{\text{p2g}} p_{t,s}^{\text{p2g}} + \sum_{t=1}^{T} c_{t,s}^{\text{ng}} p_{t,s}^{\text{ng}} + C^{\text{fix}}(x) \right) \end{aligned} \tag{21}$$

where $\gamma_{\text{prod}} = 0.8$, $C^{\text{fix}}(x)$ is the annualized CAPEX + OPEX constant term determined by x, and $\kappa_{\text{prod}}(x)$ collects conversion efficiencies and product prices (NH_3, CH_4).

(5) Carbon trading balance and piecewise decomposition

A linear emission proxy is used to keep the dispatch problem as an LP (the reported net emission accounts for CCS capture efficiency; see emission post-processing below):

$$F_s^{\text{buy}} - F_s^{\text{sell}} = \gamma_s^{\text{grid}} N_d \sum_{t=1}^{T} \left(p_{t,s}^{\text{ely}} + p_{t,s}^{\text{ng}} + p_{t,s}^{\text{p2g}} \right) - Q \tag{22}$$

where Q is the carbon quota (set to 0 in the current case study).

Piecewise decomposition:

$$\begin{aligned} F_s^{\text{buy}} &= \sum_{k=1}^{K} \delta_{k,s}^{\text{buy}}, \quad F_s^{\text{sell}} = \sum_{k=1}^{K} \delta_{k,s}^{\text{sell}} \\ 0 \le \delta_{k,s}^{\text{buy}} &\le \overline{\delta}_k, \quad 0 \le \delta_{k,s}^{\text{sell}} \le \overline{\delta}_k \end{aligned} \tag{23}$$

(6) Carbon revenue cap

Carbon revenue is constrained by the piecewise sale revenue and capped by a fraction of total cost:

$$\begin{aligned} R_s^{\text{CO2}} &\le \sum_{k=1}^{K} \pi_k^{CO2} \delta_{k,s}^{\text{sell}} \\ R_s^{\text{CO2}} &\le \gamma_{\text{CO2}} \left(\sum_{t=1}^{T} c_{t,s}^{\text{ely}} p_{t,s}^{\text{ely}} + \sum_{t=1}^{T} c_{t,s}^{\text{p2g}} p_{t,s}^{\text{p2g}} + \sum_{t=1}^{T} c_{t,s}^{\text{ng}} p_{t,s}^{\text{ng}} + C^{\text{fix}}(x) \right) \end{aligned} \tag{24}$$

To report the environmental performance, net emissions are computed by incorporating CCS capture. Let the gross hourly CO_2 emission proxy be

$$e_{t,s}^{\text{gross}} = \gamma_s^{\text{grid}} \frac{p_{t,s}^{\text{ely}} + p_{t,s}^{\text{ng}} + p_{t,s}^{\text{p2g}}}{1000}. \tag{25}$$

The CCS capture efficiency is affected by $(\theta_{NG}, \phi_{O_2})$ (oxygen fraction and gas ratio) and the upper-level capture rate decision η^{ccs}. Denote the effective capture efficiency by $\eta^{\text{ccs}}(\theta_{NG}, \phi_{O_2}) \in [0, 1]$. Then

$$e_{t,s}^{\text{net}} = e_{t,s}^{\text{gross}} - r_{\text{ccs}} \eta^{\text{ccs}}(\theta_{\text{NG}}, \phi_{\text{O}_2}) e_{t,s}^{\text{gross}} \tag{26}$$

The annual net emission is

$$E_s(x) = N_d \sum_{t=1}^{T} e_{t,s}^{\text{net}} \tag{27}$$

Collecting all the above, the lower-level scenario-wise operational optimization is:

$$y_s^*(x, \xi_s) \in \arg \min_{y_s \in \Omega(x, \xi_s)} C_s(x, y_s; \xi_s), \quad s = 1, \ldots, S, \tag{28}$$

where $\Omega(x, \xi_s)$ is defined by Equations (18)–(24) and nonnegativity constraints. This explicit formulation shows that the lower level is a genuine optimization subproblem with scenario-dependent decision variables and constraints, rather than a heuristic evaluation module.

2.4. Dynamic Risk Weight and Mean–CVaR Linearization

To capture time-varying uncertainty sensitivity during operation, a dynamic operational-layer risk coefficient β_t ($t = 1, \ldots, T$) is introduced. β_t increases during peak-load periods to reflect stronger risk aversion under higher operational stress, and decreases during off-peak periods. In the proposed framework, β_t only modifies the lower-level operational loss weighting through Equation (17), thereby shaping the distribution of scenario-wise outcomes $\{C_s(x), E_s(x)\}$,while the upper-level objectives remain in the unified mean–CVaR form.

To enable a fair benchmark under identical uncertainty realizations, a static operational risk coefficient is also defined as the time average:

$$\overline{\beta} = \frac{1}{T} \sum_{t=1}^{T} \beta_t \tag{29}$$

Thus, β_t (dynamic) and $\overline{\beta}$ (static) are alternative operational-layer settings for scenario-wise evaluation, whereas ω and α remain unchanged at the planning level.

Finally, the CVaR term used in Section 2.2 follows the Rockafellar–Uryasev (RU) representation, enabling tractable integration with evolutionary optimization by evaluating max (0,·) over scenario samples.

2.5. Stepwise Carbon Price and Carbon Revenue Cap Mechanism

To represent nonlinear carbon market regulations, a stepwise carbon price mechanism is adopted. Let $\{B_k\}$ be emission (or trading volume) thresholds and $\left\{\pi_k^{CO_2}\right\}$ be the corresponding segment prices. When net emissions exceed the quota Q, the system purchases allowances with a stepwise cost; when emissions are below Q, it obtains revenue by selling the remaining quota under the same segmented rule.

A carbon revenue upper bound ($\leq 0.8 \times$ total cost) is introduced as a policy calibration constraint to prevent unrealistic dominance of carbon trading profits under extreme price realizations. It is not intended as a methodological innovation but as a regulatory safeguard reflecting practical market design considerations:

$$R_s^{\mathrm{CO2}} \leq \gamma_{\mathrm{CO2}} \cdot \mathrm{CostTotal}_s, \quad \gamma_{\mathrm{CO2}} = 0.8, \tag{30}$$

where $\mathrm{CostTotal}_s$ denotes the corresponding annualized total-cost proxy in scenario s. The stepwise carbon trading cost is embedded into the scenario-wise operational cost $C_s(x)$, thereby influencing both expectation and CVaR components in the upper-level objectives.

The adopted tiered carbon price levels (30/80/200 ¥/tCO_2) are not intended to replicate a specific carbon market but to represent progressively increasing marginal compliance pressure under tightening regulatory conditions. The breakpoint values (1000 and 5000 tCO_2) are determined relative to the annual emission scale of the studied integrated energy park. Specifically, the baseline annual emission level of the case system ranges approximately between 4000 and 7000 tCO_2/yr under conventional operation. Therefore, the following statements are true:

1. The first interval (0–1000 tCO_2) represents mild excess emissions within controllable deviation.
2. The second interval (1000–5000 tCO_2) corresponds to moderate regulatory stress approaching the baseline annual emission scale.
3. The third interval (>5000 tCO_2) represents severe excess beyond the system's typical annual emission magnitude.

Thus, the breakpoints are scale-adaptive rather than fixed universal constants, and would be adjusted proportionally for energy parks of different emission magnitudes.

2.6. System Flexibility Index

System flexibility is used to characterize the adjustment capability of the IES in response to load fluctuations and multi-source uncertainties. The comprehensive flexibility score is defined as

$$\mathrm{Flex}(x) = w_1 \cdot f_{H_2}(\overline{H}_2) + w_2 \cdot f_{\mathrm{p2g}}(\overline{P}_{\mathrm{p2g}}) + w_3 \cdot f_{\mathrm{ren}}(P_{\mathrm{renew}}) + w_4 \cdot f_{\mathrm{NG}}(\theta_{\mathrm{NG}}), \tag{31}$$

where the terms represent hydrogen storage adaptability, P2G adjustment capability, renewable penetration ratio, and natural-gas blending flexibility. The flexibility objective is incorporated into the upper-level objective vector $F(x)$.

The flexibility index is constructed as a weighted aggregation of four normalized components: hydrogen storage adaptability, P2G regulation capability, renewable penetration contribution, and gas blending flexibility. The weighting scheme (0.3, 0.3, 0.2, 0.2)

reflects a balanced functional principle rather than arbitrary preference. Active regulation resources (hydrogen storage and P2G) are assigned slightly higher weights due to their direct dispatchability and real-time adjustment capability, while structural flexibility indicators (renewable penetration and gas blending ratio) are assigned moderate weights. A sensitivity test varying the weights within ±10% shows no structural change in Pareto-front shape, indicating robustness of the flexibility index design.

Since all sub-indices are normalized to the interval [0, 1], the chosen weights ensure comparable contributions without dominating effects from any single component.

2.7. Robustness Analysis and Anomaly Elimination Mechanism

Robustness is evaluated through 300 additional disturbance samples. For each Pareto solution x, scenario-wise cost and emission samples are generated, and a dominance-based robustness index is defined to quantify the probability that a solution remains non-dominated under random perturbations. A tolerance factor (e.g., 1.02) is applied in dominance checking. Disturbance ranges follow ±20% electricity price, ±20% gas price, ±25% carbon price, ±25% grid emission factor, and ±25% renewable output. Abnormal samples are removed via Z-score and IQR detection. The remaining Pareto solutions are ranked using TOPSIS to obtain a final robust and well-balanced scheme.

To further validate the adequacy of the scenario size for CVaR estimation at $\alpha = 0.95$, a comparison between 120 and 240 correlated scenarios was conducted. The key statistical indicators of the top 10 robust solutions are summarized in Table 1. As observed, the solution cost range, emission range, and structural indicators remain within comparable magnitudes. The overall trade-off characteristics and Pareto distribution patterns remain stable, indicating sufficient convergence of tail risk estimation under 120 scenarios for planning-level analysis.

Table 1. Comparison of key performance statistics under 120 and 240 correlated scenarios.

Scenario Number	Net Cost Range (¥/yr)	Emission Range (tCO_2/yr)	Mean Robustness	Mean Flexibility
120	6.29×10^4–2.04×10^6	27–477	0.882	0.219
240	1.24×10^5–2.25×10^6	29–535	0.775	0.272

Minor adjustments in installed capacity levels are observed, but the overall trade-off patterns between cost, emission, and flexibility remain stable. This confirms that the main conclusions are not sensitive to moderate increases in scenario count and that 120 scenarios provide a computationally efficient yet structurally reliable approximation.

3. Mathematical Modeling and Solution Algorithm

3.1. Nested Bilevel Optimization Strategy

This study employs a nested parameterized bilevel optimization strategy, where the lower-level operational problem is solved to optimality for each scenario and capacity decision. The model is not reformulated as a single-level MPEC/KKT program, but rather explicitly maintains the hierarchy through a nested evaluation mechanism.

To solve the proposed bilevel stochastic optimization problem, a nested solution strategy is adopted.

For each upper-level candidate decision x, the evaluation procedure consists of three steps:

(1) Generate uncertainty scenarios $\{\xi_S\}_{S=1}^{S}$ using Monte Carlo sampling with correlation preservation.

(2) For each scenario ξ_S, solve the lower-level operational optimization problem to obtain the optimal response $y_S^*(x)$.
(3) Compute scenario-wise outcomes $C_s(x)$ and $E_s(x)$, and aggregate them via the mean–CVaR formulation defined in Equation (5).
The aggregated objective vector $F(x)$ is then returned to the upper-level evolutionary algorithm.

It should be emphasized that Monte Carlo sampling is used only to generate uncertainty scenarios and does not replace the lower-level optimization. For each scenario, the operational problem is solved to optimality, ensuring that the upper-level evaluation strictly depends on the lower-level optimal response.

3.2. Formal Bilevel Coupling Conditions

To clarify the formal coupling between upper and lower levels, the lower-level subproblem under each scenario ξ_S can be written in a general linear form

$$\min_{y_s} c_s^T y_s \quad \text{s.t.} \quad A_s y_s \geq b_s(x, \xi_s), \quad y_s \geq 0, \tag{32}$$

Since the lower-level problem is convex (LP/convex with piecewise linear constraints), its optimality can be equivalently characterized by

(1) primal feasibility: $A_s y_s \geq b_s(x, \xi_s), \quad y_s \geq 0$;
(2) dual feasibility: $A_s^T \lambda_s \leq c_s, \quad \lambda_s \geq 0$;
(3) strong duality: $c_s^T y_s = b_s(x, \xi_s)^T \lambda_s$.

The strong duality condition ensures that

$$C_s^T y_s = b_s(x, \xi_S)^T \lambda_S \tag{33}$$

These conditions provide a formal bilevel coupling mechanism, demonstrating that the upper-level objectives are constructed based on lower-level optimal solutions rather than heuristic simulation.

In this study, instead of reformulating the bilevel problem into a single-level KKT-based mathematical program, the nested solution approach is adopted for computational efficiency while preserving theoretical rigor.

3.3. Dynamic Mean–CVaR Risk Modeling

The dynamic coefficient β_t introduced in Section 2.4 is incorporated within the lower-level scenario evaluation stage.

Specifically, β_t adjusts the time-dependent sensitivity to adverse operational conditions (e.g., peak-load periods). This modification affects the scenario-wise operational loss distribution but does not alter the unified upper-level mean–CVaR structure defined in Equation (5).

Therefore, ω governs global risk preference at planning level and β_t reflects intra-day temporal risk sensitivity.

This separation avoids duplication of risk parameters and ensures consistent notation across sections.

We further implement a same-scenario benchmarking module. Specifically, a fixed correlated scenario set $\{\xi_s\}_{s=1}^S$ is generated once (with a fixed random seed) and then reused for both the dynamic-β_t and static-β_{static} evaluations. For a given representative solution x, we compute the scenario-wise outcomes $\{C_S(x)\}$ and $\{E_S(x)\}$ under the two risk settings, and report $\mathbb{E}[\cdot]$, $\text{CVaR}_\alpha(\cdot)$ and the corresponding empirical CDFs for a tail risk comparison.

3.4. NSGA-II Integration with RU-Based Mean–CVaR Evaluation and Embedded Carbon Pricing

The upper-level planning problem is solved using NSGA-II because it can effectively handle nonlinear and nonconvex multi-objective decision spaces. In order to avoid a purely narrative coupling description, we explicitly define the fitness evaluation operator used by NSGA-II under the nested bilevel structure.

For any upper-level individual x in the NSGA-II population, a correlated uncertainty scenario set $\{\xi_S\}$ is generated, and the lower-level operational problem is solved under each scenario ξ_S to obtain the scenario-wise optimal response $y_S^*(x)$.

Note that the stepwise carbon pricing and revenue cap mechanism is embedded in the scenario-wise cost $C_s(x)$, so carbon market feedback influences both the expectation and tail risk terms.

Given $\{C_S(x)\}_{s=1}^S$ and $\{E_S(x)\}_{s=1}^S$, the RU-based CVaR definition in Equation (4) is used as an explicit evaluation sub-operator. Therefore, the risk-adjusted fitness vector returned to NSGA-II is

$$\mathrm{F}(x) = [F_1(x), F_2(x), F_3(x)] = ((1-\omega)\mathbb{E}[C(x)] + \omega \mathrm{CVaR}_\alpha(C(x)),\ (1-\omega)\mathbb{E}[E(x)] + \omega \mathrm{CVaR}_\alpha(E(x)),\ -F_{\mathrm{flex}}(x)), \quad (34)$$

where $\mathbb{E}[C(x)]$ and $\mathbb{E}[E(x)]$ are computed by Equations (4) and (5) and $CVaR_\alpha(\cdot)$ is computed by Equation (4) (and its emission counterpart). This mapping $\mathrm{F}(x)$ is evaluated for every individual in every generation and is directly used by NSGA-II for non-dominated sorting and crowding-distance-based selection.

4. Results and Discussion

4.1. Risk Weight Sensitivity Analysis and Discussion

To investigate how risk preference affects the planning outcomes, we conduct a sensitivity analysis on the global CVaR risk aversion coefficient β (dimensionless), varying it from 0.05 to 0.50. Figures 3 and 4 summarize the changes in system cost, carbon emissions, flexibility, and the Pareto boundary under different values of β. Here, β controls the overall weight of tail risk (CVaR) relative to the mean performance in the upper-level objectives, thereby reflecting the decision maker's risk appetite.

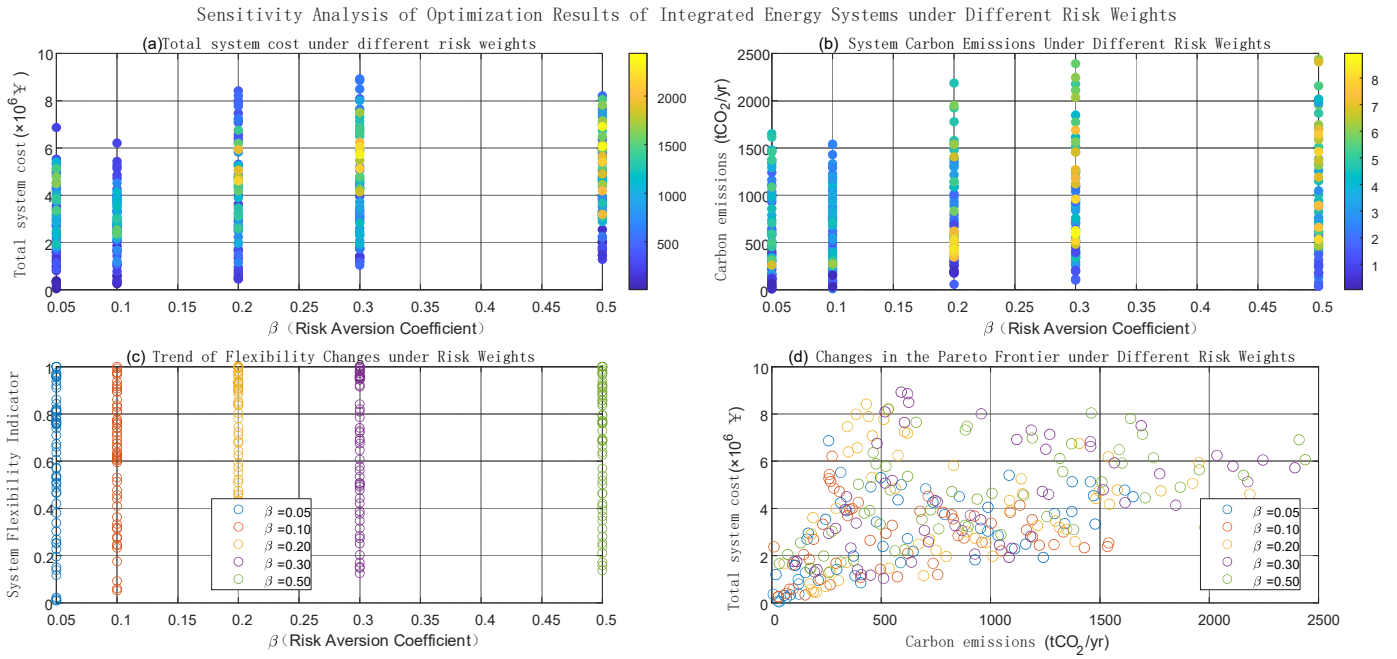


Figure 3. Sensitivity of system cost, emission, flexibility and Pareto front under different risk weights.

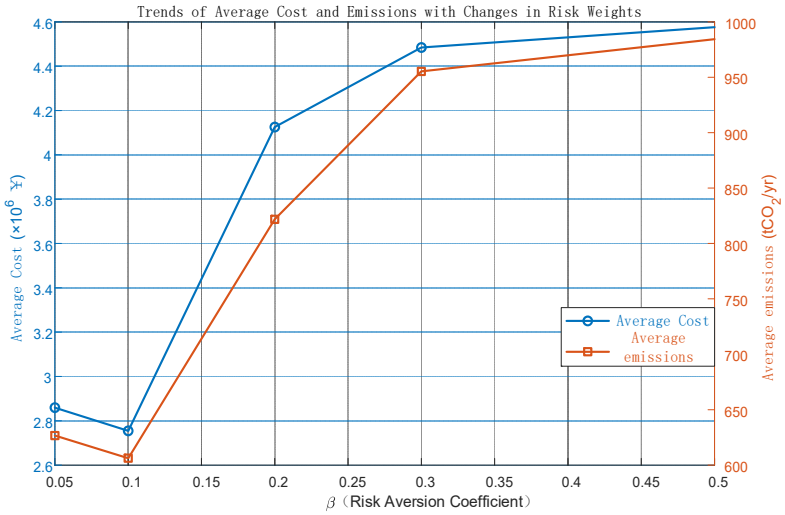
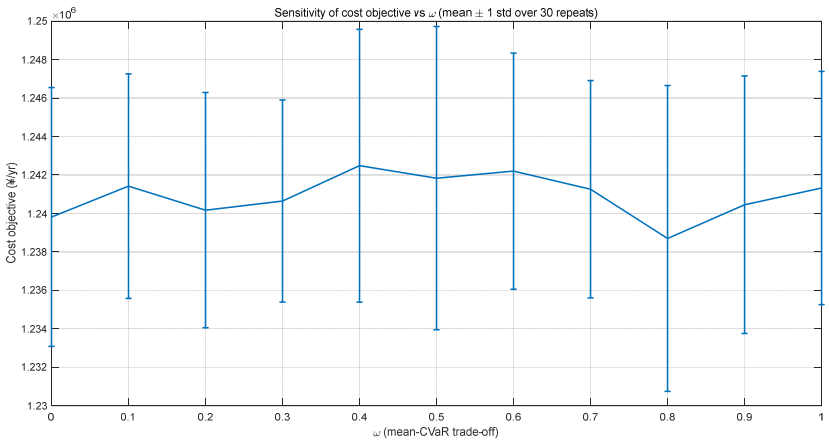
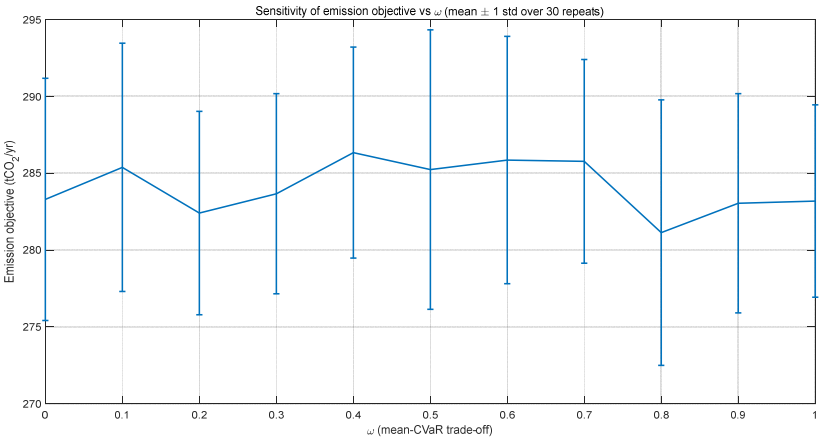


Figure 4. Trend of average cost and emissions with changes in risk weight.

In addition, since the proposed framework uses NSGA-II and scenario sampling methods for solving, the results may exhibit random fluctuations. Sensitivity assessments were independently repeated 30 times, and the mean ± one standard deviation of the mean–Conditional Value at Risk (CVaR) trade-off parameter ω was reported (Figure 5) to provide statistical confidence in the observed trends.



(**a**)



(**b**)

Figure 5. Sensitivity of the target to ω (mean ± 1 standard deviation of 30 independent repetitions). (**a**) Cost target; (**b**) emission target.

1. Impact of β on system cost and carbon emissions

Figure 3a,b illustrate the distributions of cost and emissions under different β. When β is small (e.g., 0.05–0.10), the optimization tends to produce economy-oriented solutions with relatively lower investment redundancy and hence lower total cost. As β increases (e.g., 0.30–0.50), stronger risk aversion promotes more conservative configurations (e.g., larger reserve margins and storage-related capacities), which increases the overall cost. In this regime, the optimization increasingly prioritizes worst-case/tail outcomes, and therefore shifts from purely economical operation toward risk-defensive operation.

Figure 4 further shows the average trend of cost and emissions versus β, indicating that the system performance is sensitive to risk preference, and that higher risk aversion may lead to higher expected cost due to redundancy and conservative scheduling policies.

As can be seen from Figure 3a,b, with the increase in risk weight β_t. Low β_t (0.05–0.1): the system adopts economy-oriented scheduling with cost ≈2.6–3.0 $\times$ 10^6 yuan and emissions 650–700 tCO_2/yr. High β_t (0.3–0.5): Stronger risk aversion prompts increases in hydrogen storage, electrolyzer capacity, and reserves, raising cost (>4.5 $\times$ 10^6 yuan) and emissions (~1000 tCO_2/yr).

This indicates a shift toward conservative, redundancy-focused operation under high β_t.

2. Impact of β on flexibility and Pareto-front characteristics

Figure 3c reports the flexibility index under different β. When β is small, flexibility outcomes are more dispersed, implying that the system can achieve diverse operational responses across renewable-output scenarios. As β increases beyond approximately 0.30, the flexibility distribution becomes more concentrated and the overall flexibility level tends to decrease. This suggests that strong risk aversion encourages stable and less adaptive operation, weakening the system's capability to respond to fluctuations.

From the Pareto-front comparison in Figure 3d, the boundaries corresponding to higher β shift and become steeper, indicating a tighter trade-off relationship between cost and emissions: incremental emission reduction requires disproportionately higher cost, revealing a diminishing-return characteristic in low-carbon improvements under strongly risk-averse planning.

3. Statistical robustness under ω

To evaluate whether the sensitivity trends are statistically reliable, we further examine the mean–CVaR trade-off parameter $\omega \in [0, 1]$, where larger ω places more emphasis on CVaR relative to the mean. For each ω, we perform 30 independent repeats with different random seeds and report mean $\pm$ one standard deviation.

As shown in Figure 5, both the cost objective and the emission objective exhibit weak sensitivity to ω, and the uncertainty bands largely overlap across different ω values. This implies that the observed fluctuations are not statistically strong at the current sampling resolution, and importantly, that the overall conclusions regarding the cost–emission–flexibility trade-off are robust with respect to ω. Therefore, $\omega = 0.5$ is adopted as a balanced setting in subsequent experiments.

4. Summary of sensitivity findings

Overall, increasing β transforms system operation from an economical type to a robust type, reflecting a shift from cost optimization toward tail risk protection under uncertainty. The additional ω-based repeated tests confirm that the main trends are statistically stable and are not driven by random fluctuations of NSGA-II runs or scenario sampling.

The overlapping confidence intervals indicate that the optimization trends are structurally stable and not sensitive to stochastic search randomness.

4.2. Analysis of Dynamic Risk and Carbon Price Coupling Mechanism

1. Same-scenario comparison: dynamic β_t vs. static β_{static}

Figure 6 shows the distribution curve of dynamic risk weight β_t within 24 h of a typical day. The dynamic risk weight β_t increases significantly during the period of superimposed high load and renewable-energy fluctuation (t = 16–20 h), and the model automatically increases the risk weight during the period of high uncertainty, thus making the optimization tend to choose a more robust operation strategy. Compared with the fixed β model, the variance of system cost under the dynamic β_t model decreases by about 14%, and the emission variance decreases by about 18%, which effectively suppresses the spread of extreme risks and realizes a more reasonable temporal distribution of risks.

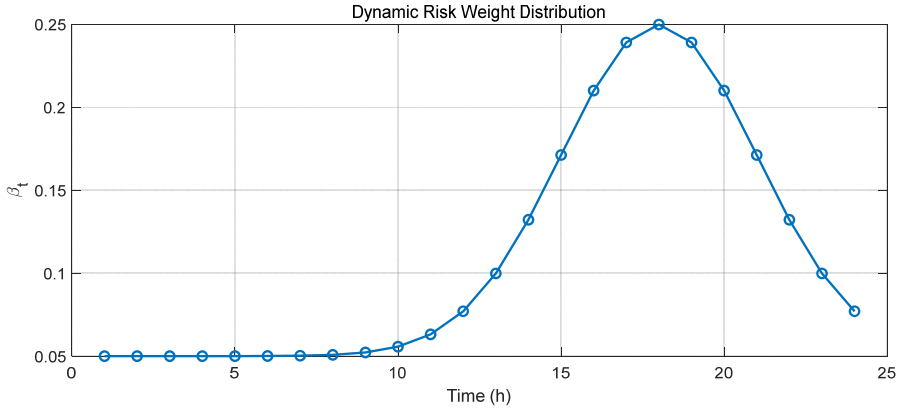


Figure 6. Temporal distribution characteristics of dynamic risk weight β_t.

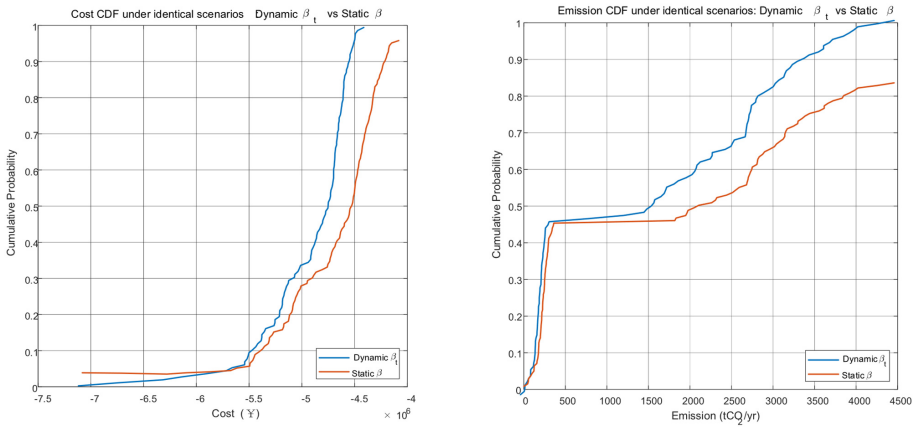
For each setting, we obtain scenario-wise samples $\{C_s(x)\}$ and $\{E_s(x)\}$ and then compute $\mathbb{E}[C]$, $\mathrm{CVaR}_\alpha(C)$, $\mathbb{E}[E]$ and $\mathrm{CVaR}_\alpha(E)$ using the same confidence level $\alpha\backslash\mathrm{alpha}\alpha$. The empirical CDFs of cost and emission under identical scenarios are further plotted to visualize tail behaviors. Results indicate that the dynamic-β_t design yields a more concentrated tail distribution compared with the static benchmark, demonstrating improved suppression of extreme-loss realizations during peak-risk periods.

The cost CDF under identical scenarios shows that the dynamic β_t configuration consistently lies to the left of the static β curve across most probability levels. This indicates that, for a given cumulative probability, the dynamic risk-weighting strategy achieves lower operating cost. In particular, in the upper tail region ($\alpha \geq 0.9$), the dynamic formulation exhibits a smaller extreme-cost realization, confirming improved tail risk suppression.

Similarly, the emission CDF demonstrates a clear leftward shift of the dynamic β_t curve compared with the static benchmark. This implies that the proposed time-varying risk mechanism effectively reduces high-emission outcomes under identical uncertainty realizations. The reduction in the dispersion of extreme-emission scenarios further validates the robustness enhancement introduced by dynamic risk weighting.

The dynamic β_t formulation does not necessarily dominate the static β case in terms of Pareto efficiency under identical scenarios. Instead, it primarily reshapes the tail risk distribution by reducing extreme cost and emission realizations while maintaining comparable expected performance.

Figure 7 illustrates the empirical cumulative distribution functions (CDFs) of system cost and emissions under identical uncertainty scenarios for the dynamic β_t and static β settings. Results indicate that the dynamic β_t design yields a more concentrated tail distribution compared with the static benchmark, demonstrating improved suppression of extreme-loss realizations during peak-risk periods.



(**a**) (**b**)

Figure 7. (**a**) Cost CDF under identical scenarios: dynamic β_t vs. static β; (**b**) Emission CDF under identical scenarios: dynamic β_t vs. static β.

2. Regulatory and incentive effects of graded carbon price mechanism

The graded carbon price mechanism has a significant guiding effect on system emission reduction behavior. When the annual emission reduction exceeds 5000 tCO_2, the carbon price increases from 80 ¥/t to 200 ¥/t, further strengthening the economic incentive under high capture rates. Meanwhile, the carbon revenue cap mechanism (revenue $\leq 0.8 \times$ Total cost) effectively prevents the "excessive distortion" of carbon trading revenue on system objectives and maintains the dynamic balance between model economy and low-carbon performance. Simulation results show that after introducing the stepwise carbon price, the average system carbon emission decreases by approximately 23% compared with the fixed carbon price benchmark scenario, and the operation duration of carbon capture devices increases by 15%, verifying the effective guiding role of carbon price signals.

3. Coupling relationship between robustness and risk propagation

Robustness of the top 10 solutions exceeds 0.7 (max 0.93). High-robustness solutions show synchronized reductions in cost and emission deviations, confirming the internal "risk–response" feedback created by dynamic CVaR weighting.

It should be noted that this study focuses on isolating the marginal effect of time-varying risk weighting within the mean–CVaR framework. Therefore, a static-β baseline is adopted as a controlled comparison. Broader stochastic programming or robust optimization benchmarks are considered valuable extensions but are beyond the scope of the present study.

4.3. Optimization Convergence Analysis

To verify the solution performance of the constructed "two-layer multi-objective robust optimization model", this paper adopts an evolutionary optimization framework based on the NSGA-II for computation. The optimization problem includes eight continuous decision variables, with the objective function being a three-dimensional vector of comprehensive cost, carbon emission, and operational flexibility. The main parameters set for the algorithm are: population size of 160, maximum number of generations of 80, and number of parallel computing cores of 4.

Figure 8 shows the evolution curves of Pareto distance and Pareto spread with iteration generations during the optimization process. It can be observed that the average Pareto distance is 1 in the initial generation (Generation 1), indicating significant differences among solutions without forming an obvious frontier. As the number of iterations increases,

the average distance rapidly decreases to below 0.03 and stabilizes after Generation 30, demonstrating that the algorithm has successfully converged to the global non-dominated frontier. Meanwhile, the Pareto spread decreases from the initial value of 1 to approximately 0.1 and remains within a small fluctuation range, indicating that the diversity and distribution uniformity of solutions are effectively preserved.

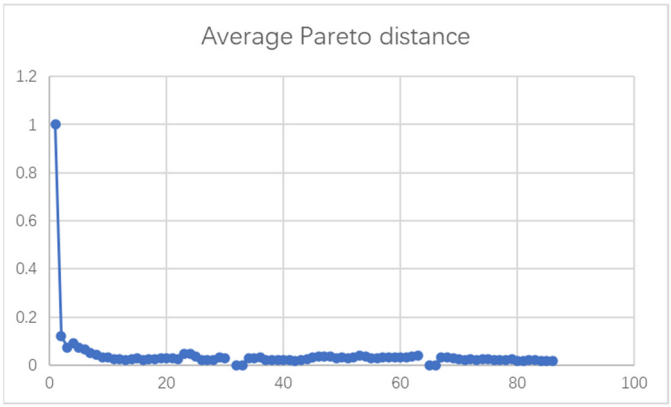


Figure 8. Pareto-front distance.

A brief sensitivity test on the carbon revenue cap coefficient (0.6–0.9) was conducted. The resulting Pareto frontier and solution ranking exhibit minor variation, and the overall trade-off characteristics remain consistent. This indicates that the main conclusions are not driven by the specific choice of the 0.8 cap parameter.

It can be concluded that the proposed bilevel multi-objective optimization algorithm exhibits excellent performance in both computational efficiency and convergence. It can obtain a stable Pareto optimal solution set within a limited number of iterations, laying a reliable foundation for subsequent multi-objective trade-off analysis.

4.4. Pareto Front and Multi-Objective Trade-Off Characteristics

Figure 9 displays the converged Pareto front. Key characteristics include the following:

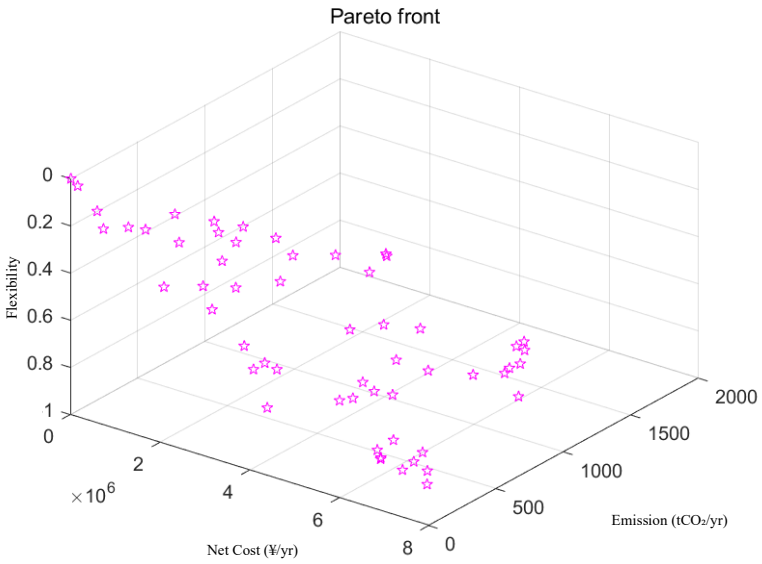


Figure 9. Distribution of the converged pareto front.

Cost–emission positive correlation: Lower cost relies on natural gas and grid electricity; lower emissions require larger renewable capacity, hydrogen storage, and CCS.

Flexibility–emission negative correlation: High flexibility depends on hydrogen storage and P2G, increasing cost but enabling deep coupling with renewables.

Figure 9 shows distribution of the converged Pareto front in the three-dimensional objective space (net cost, carbon emission, and system flexibility). Each star marker represents a non-dominated solution obtained by the NSGA-II optimization.

Overall, the Pareto frontier distribution exhibits the foll··owing typical characteristics:

Low-cost region (net cost < 5×10^5 ¥/yr) and low flexibility. Intermediate trade-off region (net cost ≈ 5×10^5–1×10^6 ¥/yr): By introducing moderate CCS and P2G units, a good balance is achieved between economy and carbon reduction performance. High-cost and low-emission region (net cost > 1×10^6 ¥/yr): The carbon capture rate is close to the upper limit (0.95), and emissions can be reduced to approximately 200 tCO_2/yr, but the cost increases significantly. In conclusion, the model in this study successfully reveals the inherent contradictions and adjustable space among economy, low-carbon performance, and flexibility in the operation of integrated energy systems, providing a basis for the quantitative design of subsequent scheduling strategies.

4.5. Top 10 Robust Solution Set and Comprehensive Performance Analysis

After obtaining the Pareto frontier, robustness verification and TOPSIS multi-index ranking of the solution set were further conducted based on Monte Carlo random perturbations (n = 300). The perturbation range includes major uncertain parameters such as electricity price, carbon price, emission factor, and equipment investment cost, with perturbation amplitudes ranging from ±20% to ±35%. The finally selected top 10 robust solutions are shown in Table 2.

Table 2. The top 10 robust capacity allocation schemes under the proposed bilevel stochastic optimization framework.

Scheme	P_renew (kW)	Elec_kW	H_2_store	CCS_rate	P2G_kW	NG_ratio	NetCost (¥)	Emission (tCO_2/yr)	Flex	Robustness
1	35.59	6.62	455.04	0.030	8.97	0.03	2.51×10^5	152.33	0.11555	0.97333
3	194.59	0.86	1366.1	0.111	6.87	0.02	4.61×10^5	92.6	0.215	0.80
5	281.5	1.20	1418.4	0.032	9.48	0.08	6.00×10^5	231.8	0.243	0.76
8	2155.6	31.60	2383.6	0.961	141.4	0.41	3.43×10^6	217.7	0.675	0.72
9	1078.4	2.04	2955.0	0.177	77.7	0.09	1.81×10^6	384.8	0.470	0.72

The 10 groups of schemes show significant differences in performance indicators, reflecting the operational diversity of the system under multi-objective constraints. Among them, Solution 1 demonstrates a combination of extremely low cost and low emissions (net cost = 2.51×10^5 yuan, emission = 152.33 tCO_2/yr), but with extremely low flexibility of only 0.0006; although this solution is numerically valid, its practical operational feasibility is weak. Solutions 3 and 5 show characteristics of balancing economic and carbon reduction performance (cost = 4.6×10^5–6.0×10^5 yuan, emission = 92–232 tCO_2/yr), with flexibility maintained in the range of 0.22–0.24, representing typical "compromise solutions". Solution 8 corresponds to the highest renewable-energy output and carbon capture rate (P_renew = 2155.6 kW, CCS_rate = 0.96), with emissions reduced to 217.7 tCO_2/yr and flexibility of 0.67, but with the highest cost (3.43×10^6 yuan); Solution 9 has the largest hydrogen storage capacity (H_2_store = 2955) and strong flexibility (Flex = 0.47), making it suitable for high-fluctuation renewable-energy scenarios.

The robustness indices of all 10 schemes are higher than 0.70, with Scheme 1 reaching 0.93 and Schemes 3 and 5 ranging between 0.76 and 0.80. This indicates that under multi-parameter perturbation conditions, the solution set can maintain stable performance without easily experiencing uncontrolled fluctuations in cost or emissions.

Further normalized visual analysis of each index through radar charts and heatmaps (Figures 10 and 11) shows that the heatmaps reflect the comprehensive performance differences of the top 10 integrated energy system schemes across four dimensions. The data has been normalized (larger values indicate better performance), and the schemes exhibit the following characteristics:

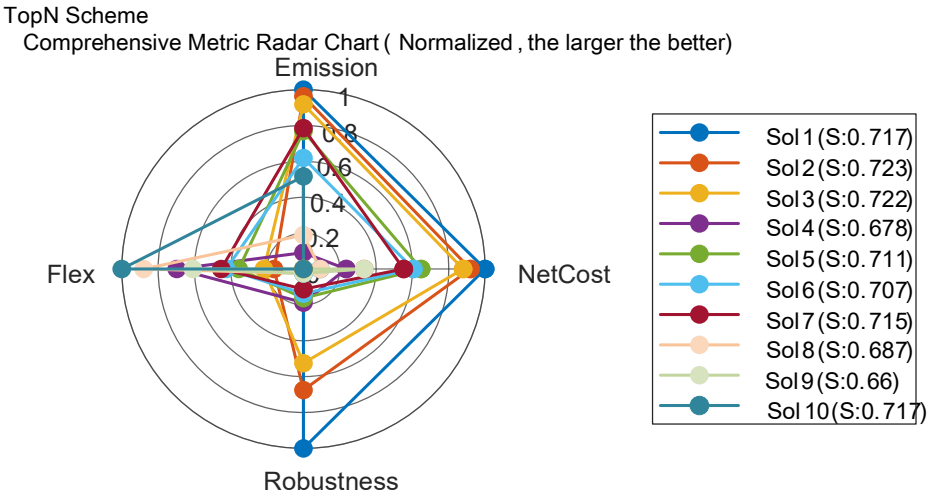


Figure 10. Top 10 radar chart.

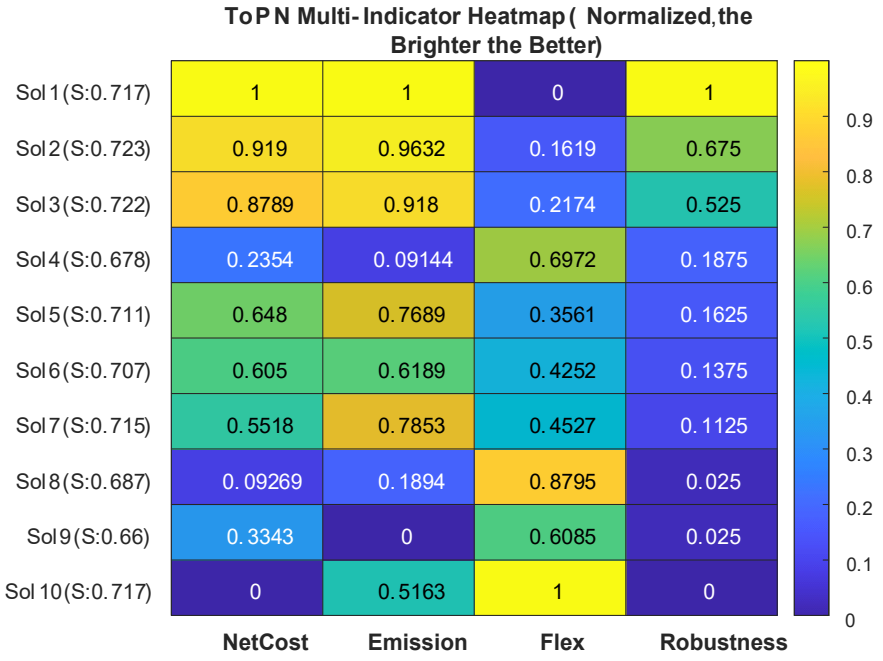


Figure 11. Top 10 heatmap.

Schemes 1, 2, 3: Both cost and emission indicators are close to 1 (optimal range), with low flexibility (<0.25) and medium-to-high robustness. The TOPSIS comprehensive score is the highest (approximately 0.72). This scenario is suitable for regions with abundant and stable wind–solar resources (such as North China, Inner Mongolia, eastern Xinjiang, etc.). The system can rely on a high proportion of renewable energy for power supply, maintaining low costs under strict carbon emission constraints. Due to stable external energy supply, the system has low dependence on the flexibility of hydrogen storage and P2G. Dominated by photovoltaic/wind energy with moderate water electrolysis hydrogen production capacity; high CCS capture rate with significant carbon market benefits; suitable as a regional clean

energy demonstration or zero-carbon park configuration scheme. Schemes 4, 8, 9: Cost and emission performance are weak (net cost and emission between 0.2 and 0.4); flexibility is high (flex approximately 0.6-0.9); robustness is low (<0.2). These scenarios are applicable to regions with significant fluctuations in wind and solar energy and obvious peak–valley load differences in power systems (such as parts of the northwest and southwest plateau regions). The system relies on large-scale hydrogen storage/P2G configurations for peak shaving and valley filling to improve renewable-energy absorption capacity. However, due to large investment scale and operational volatility, the overall stability and economy are relatively low, with a high proportion of hydrogen storage devices. The CCS capture rate is moderately reduced to save costs. These scenarios can be applied to regional peak regulation and seasonal energy storage scenarios with a high proportion of new energy. Schemes 5, 6, 7, 10: Both cost and emission levels are above average (0.5–0.8); flexibility is moderate (0.35–0.45); robustness is low but evenly distributed. The comprehensive performance is stable with scores ranging from 0.707 to 0.717. These scenarios are suitable for integrated energy systems with well-developed multi-energy coupling that prioritize both economy and low carbon, such as energy centers in urban or industrial park settings. This solution achieves a good balance among cost, emissions, and flexibility, making it suitable for integrated energy optimal operation scenarios or regional low-carbon energy hubs. It features medium-scale renewable-energy installations, balancing gas-fired power generation and electrolytic hydrogen production with moderate CCS operation efficiency (balancing energy saving and capture). It can dynamically adjust operation strategies under different market conditions (suitable for urban loads with significant seasonal variations).

Schemes 3, 5 and 8 demonstrate balanced performance across the four dimensions of cost, emission, flexibility, and robustness, forming typical "balanced optimal solutions". Relatively speaking, although Solution 1 has the lowest cost, it lacks sufficient flexibility and practical operability; while Scheme 9 exhibits outstanding flexibility, it has relatively high emissions and cost.

Based on sample statistics of the top 10 solutions, the average cost range is approximately (0.5×10^6–6.3×10^6) yuan, and the emission range is (24–1400) tCO_2/yr, with standard deviations of approximately 8% and 15% respectively, which further verifies the stability of the model's multi-solution distribution.

5. Conclusions and Discussion

5.1. Main Research Conclusions

This study developed a bilevel stochastic optimization framework for low-carbon operation of integrated electricity–hydrogen–carbon energy systems. The proposed model integrates dynamic mean–CVaR risk modeling with a stepwise carbon pricing mechanism under correlated multi-source uncertainties.

The main findings can be summarized as follows:

(1) A formally coupled bilevel stochastic structure was established, in which upper-level planning decisions are evaluated through scenario-wise optimal responses of the lower-level operational problem. The nested solution strategy preserves theoretical bilevel consistency while maintaining computational tractability.

(2) The introduction of dynamic time-varying risk coefficients enables differentiated risk sensitivity across peak and off-peak periods. Compared with static risk settings under identical uncertainty realizations, the dynamic formulation modifies tail risk distributions and alters investment–operation trade-offs.

(3) The embedded stepwise carbon pricing and revenue cap mechanism effectively regulates excessive carbon revenue distortion and strengthens emission reduction incen-

tives. Simulation results indicate that progressive carbon pricing reduces average emissions by approximately 23% relative to fixed-price benchmarks.

(4) Sensitivity analysis reveals that increasing risk aversion shifts system strategy from economy-oriented dispatch to robustness-oriented configuration, resulting in higher renewable penetration and hydrogen storage capacity but increased total cost.

(5) The multi-objective Pareto frontier demonstrates explicit trade-offs among cost, emissions, and flexibility, providing quantitative guidance for carbon market policy design and integrated energy planning.

Overall, the proposed framework offers a systematic approach for integrating stochastic risk management and carbon market regulation into bilevel energy system optimization.

5.2. Discussion and Implications

1. Importance of risk dynamics

Traditional CVaR models only measure extreme risks under static assumptions, while this paper reflects the temporal variation in risks through the dynamic β_t function. The results show that risk weighting during peak periods can effectively smooth cost fluctuations, providing inspiration for future real-time optimization.

2. Boundary effect of interaction between policy constraints and market mechanisms

The graded carbon price mechanism establishes an effective balance between low-carbon incentives and economic pressures. However, when the carbon price rises to 200 yuan/tCO_2, the marginal emission reduction efficiency of the system decreases significantly, indicating that a single price mechanism needs to be designed in coordination with technology investment, carbon quota trading, etc.

3. There exists a trade-off relationship between flexibility and robustness

The model results show that although adding flexible equipment (hydrogen storage, P2G) improves the system's ability to resist uncertainties, its economy is suppressed under high-risk-aversion scenarios. In the future, a phased depreciation model for flexible assets may be considered to further enhance the long-term feasibility of operation strategies.

4. Model generalization

The proposed method is not only applicable to electricity–gas–hydrogen–carbon integrated systems but can also be extended to low-carbon scheduling studies of multi-region integrated energy systems, especially in the context of coupling between carbon markets and green electricity trading, showing strong application potential.

5.3. Future Research Directions

1. Introduce a carbon emission path tracking mechanism to realize the coupling of intraday and annual carbon constraints.
2. Incorporate reinforcement learning algorithms to perform adaptive updates on the dynamic risk weight β_t.
3. Extend the model to multi-region interaction scenarios to study carbon transfer and risk diffusion effects.
4. This study focuses on planning-level capacity configuration under correlated uncertainty. Detailed equipment-level dynamics, such as hydrogen degradation effects, electrolyzer part load efficiency curves, and P2G ramp rate constraints, are not explicitly modeled. Incorporating such nonlinear dynamic behaviors may improve operational realism and will be considered in future research.

Author Contributions: All authors contributed to the conception and design of the study. The paper's conception was done by J.Z. and X.H.; material preparation and analysis were performed by J.L., D.C. and Y.Y. The modeling, data analysis, and drafting of the manuscript were carried out by S.C., X.C. and F.Z., and all authors provided comments on previous versions of the manuscript. All authors have read and agreed to the published version of the manuscript.

Funding: This work was supported by the Science and Technology Project of Taizhou Hongyuan Electric Power Design Institute Co., Ltd. (521186250001).

Data Availability Statement: The data presented in this study are available upon reasonable request from the corresponding author. The data are not publicly available due to confidentiality agreements with the industrial partner.

Conflicts of Interest: Authors Jing Zhang, Xinyi He, Jianfei Li, Diyu Chen and Yingang Ye were employed by the company [Taizhou Hongyuan Electric Power Design Institute Co., Ltd., Taizhou]. The remaining authors declare that the research was conducted in the absence of any commercial or financial relationships that could be construed as a potential conflict of interest. The authors declare that this study received funding from Taizhou Hongyuan Electric Power Design Institute Co., Ltd. (521186250001). The funder was not involved in the study design, collection, analysis, interpretation of data, the writing of this article, or the decision to submit it for publication.

References

1. Faisal, S.; Gao, C. A comprehensive review of integrated energy systems considering power-to-gas technology. *Energies* **2024**, *17*, 4551. [CrossRef]
2. Liang, T.; Chai, L.; Tan, J.; Jing, Y.; Lv, L. Dynamic optimization of an integrated energy system with carbon capture and power-to-gas interconnection: A deep reinforcement learning-based scheduling strategy. *Appl. Energy* **2024**, *361*, 123390. [CrossRef]
3. Fambri, G.; Diaz-Londono, C.; Mazza, A.; Badami, M.; Weiss, R. Power-to-Gas in gas and electricity distribution systems: A comparison of different modeling approaches. *J. Energy Storage* **2022**, *55*, 105454. [CrossRef]
4. Yang, C.; Dong, X.; Wang, G.; Lv, D.; Gu, R.; Lei, Y. Low-carbon economic dispatch of integrated energy system with CCS-P2G-CHP. *Energy Rep.* **2024**, *12*, 42–51. [CrossRef]
5. Zeng, Y. Low-carbon Economic Dispatch of Integrated Electricity and Heat Energy System Considering Carbon Captureand Carbon Trading Mechanism. *J. Electr. Power* **2025**, *40*, 11–24. [CrossRef]
6. Brodnicke, L.; Gabrielli, P.; Sansavini, G. Impact of policies on residential multi-energy systems for consumers and prosumers. *Appl. Energy* **2023**, *344*, 121276. [CrossRef]
7. Mu, Y.; Wang, C.; Cao, Y.; Jia, H.; Zhang, Q.; Yu, X. A CVaR-based risk assessment method for park-level integrated energy system considering the uncertainties and correlation of energy prices. *Energy* **2022**, *247*, 123549. [CrossRef]
8. Liu, C.; Guo, Q.R.; Ge, H.; Yang, Y.; Liu, Z.Y.; Gong, L. Optimal scheduling strategy for virtual power plants considering CVaR and carbon trading cost under multi-scenario conditions. *J. Electr. Eng. Autom.* **2025**, *4*, 21–40. [CrossRef]
9. Rockafellar, R.T.; Uryasev, S. Conditional Value-at-Risk for General Loss Distributions. *J. Bank. Financ.* **2002**, *26*, 1443–1471. [CrossRef]
10. Morales, J.M.; Conejo, A.J.; Pérez-Ruiz, J. Economic Valuation of Reserves in Power Systems with High Penetration of Wind Power. *IEEE Trans. Power Syst.* **2009**, *24*, 900–910. [CrossRef]
11. Moazeni, S.; Powell, W.B.; Hajimiragha, A.H. Mean-Conditional Value-at-Risk Optimal Energy Storage Operation in the Presence of Transaction Costs. *IEEE Trans. Power Syst.* **2014**, *30*, 1222–1232. [CrossRef]
12. Xuan, A.; Shen, X.; Guo, Q.; Sun, H. A conditional value-at-risk based planning model for integrated energy system with energy storage and renewables. *Appl. Energy* **2021**, *294*, 116971. [CrossRef]
13. Zhang, M.; Dong, J. Stochastic Scheduling Model for Flexible Integrated Energy System Based on CVaR. *J. Glob. Energy Interconnect.* **2020**, *3*, 301–309. [CrossRef]
14. Huang, Q.; Cheng, H.; Zhuang, Z.; Duan, M.; Fang, K.; Huang, Y.; Wang, L. Distributed Dispatch of Distribution Network Operators, Distributed Energy Resource Aggregators, and Distributed Energy Resources: A Three-Level Conditional Value-at-Risk Optimization Model. *Inventions* **2024**, *9*, 117. [CrossRef]
15. Guo, X.; Ryan, S.M. Avoiding momentum crashes using stochastic mean-CVaR optimization with time-varying risk aversion. *Eng. Econ.* **2023**, *68*, 3. [CrossRef]
16. Zhu, J.; Li, G.; Guo, Y.; Chen, J.; Liu, H.; Luo, Y. Real-time risk-averse dispatch of an integrated electricity and natural gas system via conditional value-at-risk-based lookup-table approximate dynamic programming. *Prot. Control Mod. Power Syst.* **2024**, *9*, 47–60. [CrossRef]

17. Jana, S.; Sabine, F.; Nikolay, K.; Michael, O. A dynamic CVaR-portfolio approach using real options: An application to energy investments. In Proceedings of the 2009 6th International Conference on the European Energy Market, Leuven, Belgium, 27–29 May 2009; pp. 1–7. [CrossRef]
18. Zhou, X.; Hu, J.; Li, C.; Yang, C. Risk adjustable optimal operation for electricity-hydrogen integrated energy system based on chance constrained goal programming. *J. Cent. South Univ.* **2025**, *32*, 2224–2238. [CrossRef]
19. Ran, J.; Song, Y.; Zhou, S.; Yang, K.; Liu, J.; Tian, Z. A bi-level optimization method for regional integrated energy system considering uncertainty and load prediction under climate change. *J. Build. Eng.* **2024**, *84*, 108527. [CrossRef]
20. Aljohani, T.; Mohamed, M.A.; Mohammed, O. Tri-level hierarchical coordinated control of large-scale EVs charging based on multi-layer optimization framework. *Electr. Power Syst. Res.* **2024**, *226*, 109923. [CrossRef]
21. Zhao, J.; Liu, Y.; Chen, A. Modeling robust bi-level BCC production planning problem with uncertain carbon emission mechanism. *Comput. Chem. Eng.* **2024**, *181*, 108548. [CrossRef]
22. Li, H.; Ye, Y.; Lin, L. Low-Carbon Economic Bi-Level Optimal Dispatching of an Integrated Power and Natural Gas Energy System Considering Carbon Trading. *Appl. Sci.* **2021**, *11*, 6968. [CrossRef]
23. Lu, M.; Teng, Y.; Chen, Z.; Song, Y. A bi-level optimization strategy of electricity-hydrogen-carbon integrated energy system considering photovoltaic and wind power uncertainty and demand response. *Sci. Rep.* **2025**, *15*, 18. [CrossRef] [PubMed]
24. Zhou, S.; Han, Y.; Zalhaf, A.S.; Lehtonen, M.; Darwish, M.M.F.; Mahmoud, K. Risk-averse bi-level planning model for maximizing renewable energy hosting capacity via empowering seasonal hydrogen storage. *Appl. Energy* **2024**, *361*, 122853. [CrossRef]
25. Wang, L.; Ren, X.; Ma, Y.; Liu, Z.; Dong, W.; Ni, L. Optimal low-carbon scheduling of integrated energy systems considering stepped carbon trading and source-load side resources. *Energy Rep.* **2024**, *12*, 3145–3154. [CrossRef]
26. Xu, T.; Cheng, C.; Ren, F.; Zhang, W. Optimal scheduling of integrated energy systems considering carbon trading. *J. Phys. Conf. Ser.* **2022**, *2395*, 012053. [CrossRef]
27. Tanveer, U.; Ishaq, S.; Hoang, T.G. Enhancing carbon trading mechanisms through innovative collaboration: Case studies from developing nations. *J. Clean. Prod.* **2024**, *482*, 144122. [CrossRef]
28. Kong, X.; Zheng, Y.; Yang, S.; Wang, Y. Profit-driven economic expansion planning of CCUS deployment and carbon trading in carbon-neutral energy systems under liberalized market-oriented decarbonization strategies with step-based pricing. *Energy* **2025**, *334*, 136762. [CrossRef]
29. Jiang, X.; Lv, S.; Wang, J.; Zhang, Y.; Bao, Z.; Yu, M. Park-level Integrated Energy System Planning Considering Tiered Carbon Trading and Optimal Construction Timing Under Dual Carbon Goals. *Electr. Meas. Instrum.* **2023**, *60*, 11–19. [CrossRef]
30. Zhang, N.; Jia, J.X.; Li, B.Q.; Shi, Z. Study on optimization of operation strategy of electric-gas coupling virtual power plant considering carbon trading. *Electr. Meas. Instrum.* **2024**, *61*, 20–28. [CrossRef]
31. Minai, A.F.; Khan, A.A.; Kitmo; Ndiaye, M.F.; Alam, T.; Khargotra, R.; Singh, T. Evolution and role of virtual power plants: Market strategy with integration of renewable-based microgrids. *Energy Strategy Rev.* **2024**, *53*, 101390. [CrossRef]
32. Mashhour, E.; Moghaddas-Tafreshi, S.M. Bidding strategy of virtual power plant for participating in energy and spinning reserve markets—Part I: Problem formulation. *IEEE Trans. Power Syst.* **2011**, *26*, 949–956. [CrossRef]
33. Zhao, F.; Wang, Y. IES optimal scheduling with carbon trading mechanism and coupled demand response. *Mod. Electron. Tech.* **2025**, *48*, 91–98. [CrossRef]

Disclaimer/Publisher's Note: The statements, opinions and data contained in all publications are solely those of the individual author(s) and contributor(s) and not of MDPI and/or the editor(s). MDPI and/or the editor(s) disclaim responsibility for any injury to people or property resulting from any ideas, methods, instructions or products referred to in the content.